

# Highly Reversible Open Framework Nanoscale Electrodes for Divalent Ion Batteries

Richard Y. Wang,<sup>†</sup> Colin D. Wessells,<sup>†</sup> Robert A. Huggins,<sup>†</sup> and Yi Cui<sup>\*,†,‡</sup>

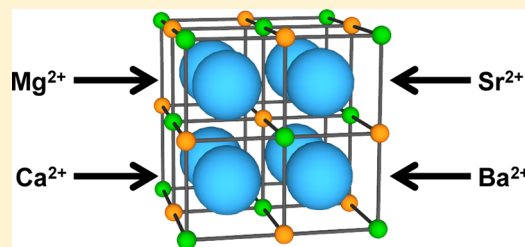
<sup>†</sup>Department of Materials Science and Engineering, Stanford University, Stanford, California 94305, United States

<sup>‡</sup>Stanford Institute for Materials and Energy Sciences, SLAC National Accelerator Laboratory, 2575 Sand Hill Road, Menlo Park, California 94025, United States

**S** Supporting Information

**ABSTRACT:** The reversible insertion of monovalent ions such as lithium into electrode materials has enabled the development of rechargeable batteries with high energy density. Reversible insertion of divalent ions such as magnesium would allow the creation of new battery chemistries that are potentially safer and cheaper than lithium-based batteries. Here we report that nanomaterials in the Prussian Blue family of open framework materials, such as nickel hexacyanoferrate, allow for the reversible insertion of aqueous alkaline earth divalent ions, including  $\text{Mg}^{2+}$ ,  $\text{Ca}^{2+}$ ,  $\text{Sr}^{2+}$ , and  $\text{Ba}^{2+}$ . We show unprecedented long cycle life and high rate performance for divalent ion insertion. Our results represent a step forward and pave the way for future development in divalent batteries.

**KEYWORDS:** Ion insertion, magnesium ion batteries, aqueous batteries, Prussian Blue, open framework structure, nanomaterials



Rechargeable battery technologies have enabled the continuing development of electronics and transportation with great promise toward vehicle electrification and grid-scale energy storage.<sup>1–7</sup> Monovalent ion intercalation of protons and lithium ions into solid materials has led to the success of nickel metal hydride and lithium ion rechargeable batteries.<sup>8,9</sup> Recently, divalent magnesium ion insertion has attracted great interest due to magnesium's low cost, elemental abundance, and doubling of electron storage capacity per ion compared to lithium.<sup>10–12</sup> Studies have demonstrated magnesium insertion in metal chalcogenides, transition metal oxides, and olivines<sup>11–14</sup> but finding an electrode material with fast, reversible insertion of divalent magnesium ions remains a major challenge.

We explored Prussian Blue (PB) open framework nanomaterials for divalent ion insertion because of their interesting crystal structure. The general formula for these materials is  $\text{A}_x\text{PR}(\text{CN})_6 \cdot y\text{H}_2\text{O}$ , and their crystal structure (Figure 1A) is analogous to that of the  $\text{ABX}_3$  perovskites. The  $\text{P}^{m+}$  and  $\text{R}^{n+}$  ions form an ordered arrangement on the B sites.<sup>15,16</sup> The triple-bonded CN ligands increase the separation between P and R ions to open up the structure for ion and small molecule insertion. The occupancy of the tetrahedrally coordinated A sites in the large open cages in this crystallographically nanoporous framework (Figure 1A) varies from  $x = 0$  to 2 per formula unit with corresponding changes in the oxidation states of P and R ions. As a result of these structural characteristics, these materials are mixed ionic and electronic conductors.<sup>17</sup> In addition, zeolitic water in the A sites and on vacant nitrogen sites can facilitate ion insertion.<sup>18,19</sup>

The structure and physical properties of PB materials have been studied extensively.<sup>15,16,18,20–23</sup> Electrodeposited PB thin

films have demonstrated reversible insertion of potassium ions in aqueous solution for electrochromic window applications.<sup>24–26</sup> Recently, nanomaterials in the PB family have been explored for monovalent batteries; this includes potassium, sodium, and lithium ion batteries in both aqueous and organic solutions.<sup>19,27–33</sup> In particular, both nickel and copper hexacyanoferrate (NiHCF, CuHCF) demonstrate high cycling rates with excellent capacity and cycle life retention through reversible insertion of  $\text{K}^+$  and  $\text{Na}^+$  cations.<sup>27,28</sup> In addition, the effects of different monovalent insertion cations on hexacyanoferrate performance<sup>34</sup> and the tunability of reaction potential by forming a nickel–copper hexacyanoferrate alloy<sup>35</sup> have been studied.

Success with monovalent ion insertion has motivated us to explore these materials for divalent insertion. Past research on PB thin films suggests divalent alkaline earth cations ( $\text{Mg}^{2+}$ ,  $\text{Ca}^{2+}$ ,  $\text{Sr}^{2+}$ ,  $\text{Ba}^{2+}$ ) can reversibly insert into these materials.<sup>36,37</sup> However, those studies did not investigate the potential of these materials for batteries and failed to demonstrate high rates or cycle life performance because of the use of thin films, which present poor ionic conductance relative to that in nanoscale materials. In this work, we demonstrate unprecedented high-rate cycling of nanoscale NiHCF electrodes with  $\text{Mg}^{2+}$ ,  $\text{Ca}^{2+}$ ,  $\text{Sr}^{2+}$ , and  $\text{Ba}^{2+}$  ions with long cycle life and promising energy efficiency.

NiHCF nanoparticles were synthesized by a coprecipitation method<sup>28</sup> with slow, simultaneous dropwise addition of 70 mL each of aqueous nickel nitrate and potassium ferricyanide solutions (Sigma-Aldrich) into 60 mL of deionized water at 80

**Received:** October 1, 2013

**Published:** October 22, 2013

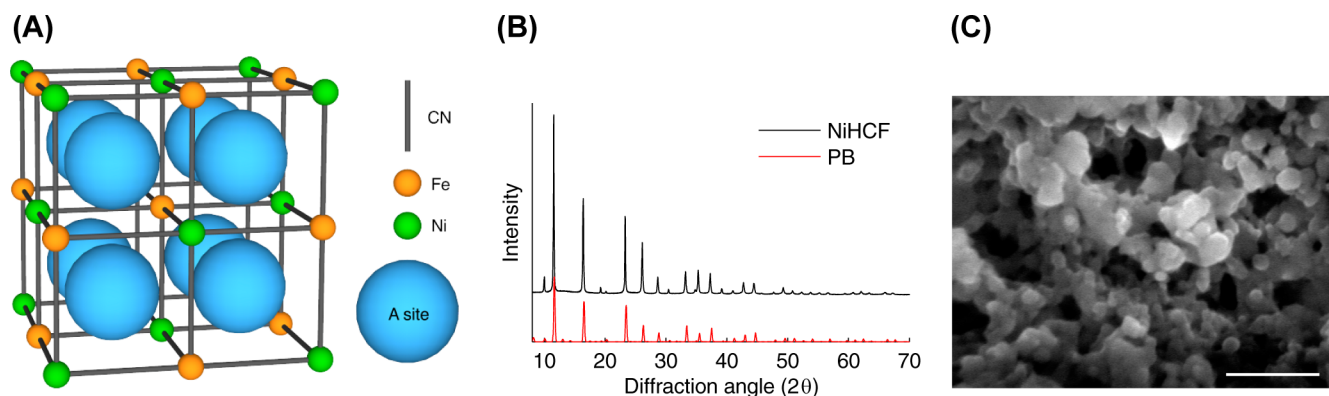


**Figure 1.** (A) NiHCF shares the same cubic open framework structure with Prussian Blue.  $\text{Ni}^{2+}$  occupies the nitrogen-coordinated P sites, and  $\text{Fe}^{3+}$  occupies the carbon-coordinated R sites. Insertion cations and zeolitic water occupy the A sites in each subcell of the unit cell. The open channels in the  $\langle 100 \rangle$  directions allow for rapid insertion and extraction of a variety of cations. (B) The X-ray powder diffraction pattern of NiHCF demonstrates the high crystallinity and phase purity of the material used in this study. All peaks match up with the reference Prussian Blue phase.<sup>16</sup> (C) The scanning electron micrograph shows nanoparticles of NiHCF ranging from 30 to 70 nm (scale bar = 200 nm).

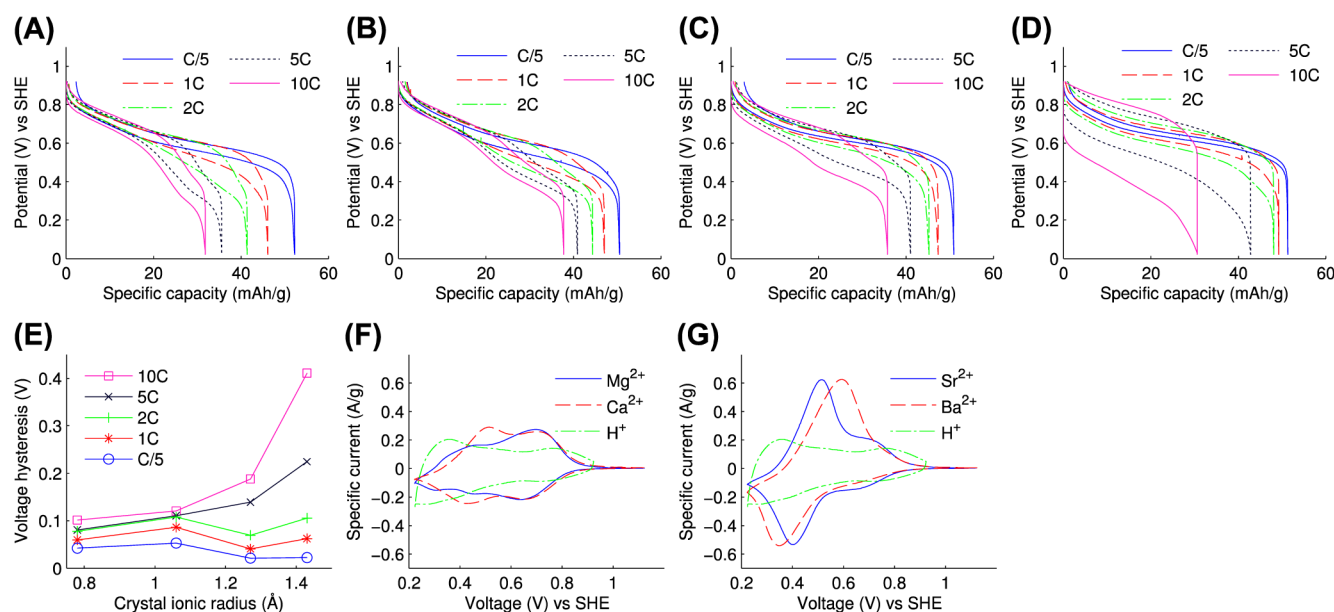


**Figure 2.** (A–D) Potential profiles of NiHCF upon galvanostatic cycling with  $\text{Mg}^{2+}$ ,  $\text{Ca}^{2+}$ ,  $\text{Sr}^{2+}$ , and  $\text{Ba}^{2+}$ , respectively, exhibit decreasing capacity and increasing voltage hysteresis with C rate. The kinked profiles at high C rates may be the result of a two-step diffusion-limited insertion reaction that is the subject of further study. (E) The voltage hysteresis at half charge increases monotonically with C rate. This increase in hysteresis tends to be greater for cations with larger crystal ionic radii. (F–G) Cyclic voltammetry (CV) curves demonstrate reversible insertion of  $\text{Mg}^{2+}$ ,  $\text{Ca}^{2+}$ ,  $\text{Sr}^{2+}$ , and  $\text{Ba}^{2+}$ , and they suggest two insertion reactions occurring at different potentials. CV curves of NiHCF cycled with dilute nitric acid at pH 2 show that  $\text{H}^{+}$  insertion does not account for the observed electrochemistry.

$^{\circ}\text{C}$  for final concentrations of 40 mM nickel nitrate and 20 mM potassium ferricyanide. The solid precipitate was vacuum filtered from the solution, washed, and dried under vacuum at room temperature. This synthesis procedure produces phase-pure NiHCF with high crystallinity and nanoparticle morphology as confirmed by powder X-ray diffraction (XRD) and scanning electron microscopy (Figure 1B,C). The XRD pattern was collected at the Stanford Synchrotron Radiation Light-source with Bragg–Brentano geometry using a monochromator at 12 keV.

Most electrochemical measurements were performed in a three-electrode flooded half cell configuration with a NiHCF carbon cloth working electrode, a  $\text{Ag}/\text{AgCl}$  reference electrode (Fisher Scientific), and a platinum counter electrode (Fisher Scientific). NiHCF electrodes were fabricated by mixing 80% w/w NiHCF, 9% w/w polyvinylidene fluoride (Kynar), 9% w/w

w amorphous carbon (Timcal), and 2% w/w graphite (Timcal) and grinding the components together with a mortar and pestle.<sup>28</sup> The powder was mixed with 1-methyl-2-pyrrolidinone (Sigma-Aldrich) to create a slurry that was deposited onto carbon cloth current collectors (Fuel Cell Earth). These electrodes were dried under vacuum at  $80^{\circ}\text{C}$  and exhibited a typical mass loading of approximately  $10\text{ mg}/\text{cm}^2$ .

Measurements of cycle life were performed in a full cell setup with an activated carbon counter electrode.<sup>29</sup> Activated carbon counter electrodes used for long-term cycling were fabricated by mixing together 80% w/w activated carbon (Sigma Aldrich) and 20% w/w polyvinylidene fluoride (Kynar), grinding the components together with a mortar and pestle, and combining with 1-methyl-2-pyrrolidinone to form a slurry. The slurry was deposited onto carbon cloth current collectors (Fuel Cell Earth) and dried under vacuum at  $80^{\circ}\text{C}$ . Typical mass loading

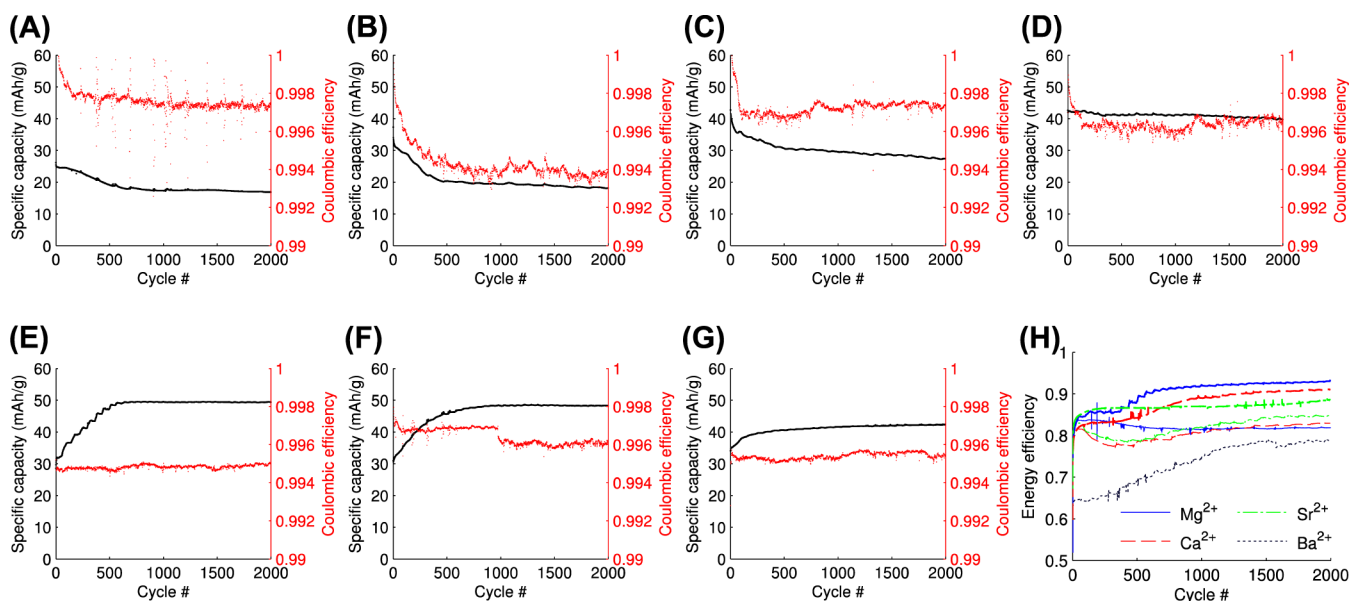


**Figure 3.** (A–D) The specific capacity (black line) at 5C decays at different rates for Mg<sup>2+</sup>, Ca<sup>2+</sup>, Sr<sup>2+</sup>, and Ba<sup>2+</sup> electrolytes, respectively. In all cases, the capacity stabilizes after the electrode stops dissolving as the electrolyte becomes saturated with dissolved Ni<sup>2+</sup>. Coulombic efficiency (red dotted line) ranges from 99.4 to 99.8%. (E–G) When 20 mM Ni<sup>2+</sup> is added to the electrolyte before cycling, specific capacity retention improves significantly for Mg<sup>2+</sup>, Ca<sup>2+</sup>, and Sr<sup>2+</sup>, respectively. (H) Energy efficiency improves when adding Ni<sup>2+</sup> to the electrolyte. The thicker lines indicate cells with Ni<sup>2+</sup>.

for these electrodes was approximately 50–100 mg/cm<sup>2</sup>. Aqueous electrolytes were prepared by dissolving the appropriate metal nitrates in deionized water to 0.1 M for Ba<sup>2+</sup> and 1 M for all other cations. A pH of 2 was maintained in all electrolytes by adding nitric acid to increase the acidity. All C rates are calculated assuming a maximum specific capacity of 50 mAh/g for NiHCF.

The nominal chemical formula of NiHCF in its oxidized state is KNiFe<sup>3+</sup>(CN)<sub>6</sub> with half of the A sites filled with potassium ions. Ni<sup>2+</sup> occupies the nitrogen-coordinated P sites, and Fe<sup>3+</sup> occupies the carbon-coordinated R sites (Figure 1A). Upon reduction of the material during discharge, alkaline earth ions (M<sup>2+</sup>, M = Mg, Ca, Sr, Ba) enter the structure to produce KM<sub>x</sub>Ni[Fe<sup>2+</sup>(CN)<sub>6</sub>]<sub>2x</sub>[Fe<sup>3+</sup>(CN)<sub>6</sub>]<sub>1–2x</sub>.

The sloping potential profiles of Mg<sup>2+</sup>, Ca<sup>2+</sup>, Sr<sup>2+</sup>, and Ba<sup>2+</sup> insertion into NiHCF indicate single-phase reactions during charge and discharge at C/5, which correlates with previous studies of K<sup>+</sup> and Na<sup>+</sup> insertion into NiHCF<sup>28</sup> (Figure 2A–D). For Mg<sup>2+</sup>, Ca<sup>2+</sup>, Sr<sup>2+</sup>, and Ba<sup>2+</sup>, the half-charge reaction potentials versus SHE are 0.60, 0.59, 0.63, and 0.64 V, respectively. There is a distinct second plateau in the potential profile at high C rates when the electrodes are discharged beyond roughly 50% of total capacity in Mg<sup>2+</sup>, Ca<sup>2+</sup>, or Sr<sup>2+</sup>. This suggests a two-step insertion reaction, but the precise mechanism of insertion for these divalent cations is presently unknown. The retention of specific capacity with increasing charge rate is much higher than previously reported for magnesium electrodes<sup>11</sup> with retention of specific capacity of 63, 77, 70, and 60% going from C/5 to 10C for Mg<sup>2+</sup>, Ca<sup>2+</sup>, Sr<sup>2+</sup>, and Ba<sup>2+</sup>, respectively. Both the high ionic conductivity of NiHCF and the short diffusion pathways within the nanoparticles contribute to the rapid kinetics.

Increasing the charge and discharge rates increases the voltage hysteresis for all electrolytes tested but it is exciting to see that the hysteresis is remarkably small. From C/5 to 10C (a 50-fold increase in charge and discharge rates), the voltage

hysteresis at half charge increases only by 59, 68, 167, and 388 mV, respectively, for Mg<sup>2+</sup>, Ca<sup>2+</sup>, Sr<sup>2+</sup>, and Ba<sup>2+</sup>. As the charge/discharge rates go up, the increase in voltage hysteresis scales with the unhydrated crystal ionic radius of the cation (Figure 2E) even though these insertion ions are typically hydrated both inside and outside the crystal lattice.<sup>18</sup> This might indicate a rate-limiting dehydration step during insertion, which is consistent with past studies on divalent ion insertion in PB analogues.<sup>37</sup> Studies have also shown a relationship between the hydration energy of insertion ions and their formal insertion potential, which suggests a dehydration step during insertion.<sup>38</sup> Data on electrochemical impedance spectroscopy for NiHCF in these electrolytes, which corresponds to the charge transfer resistance associated with dehydration of the ions, can be found in the Supporting Information. Ongoing in situ synchrotron X-ray diffraction and neutron diffraction studies in our group could provide a more complete understanding of the insertion mechanism for divalent cations into NiHCF in the future.

Cyclic voltammograms (CVs) show reversible insertion of Mg<sup>2+</sup>, Ca<sup>2+</sup>, Sr<sup>2+</sup>, and Ba<sup>2+</sup> ions within the stability range of the aqueous electrolyte (Figure 2F–G) and also demonstrate the presence of two insertion reactions at different potentials with these alkaline earth electrolytes. CVs taken in dilute nitric acid at pH 2 show that H<sup>+</sup> insertion does not account for the major electrochemical features observed in NiHCF. Inductively coupled plasma optical emission spectroscopy (ICP-OES) of specially prepared dilute electrolytes (2.6 mM divalent cations, pH 4) before and after reduction of the cathode provides further qualitative evidence that these divalent ions are inserting into the electrode material. The decrease in insertion ion concentration of the electrolytes after electrode discharge reached 11, 41, 64, and 73% of what would be expected based on the discharge capacities for electrodes in Mg<sup>2+</sup>, Ca<sup>2+</sup>, Sr<sup>2+</sup>, and Ba<sup>2+</sup> electrolytes, respectively. The use of especially dilute electrolytes, which may lead to incomplete insertion of ionic species, likely accounts for much of the discrepancy between



theoretical and observed values. These results do not rule out partial insertion of hydronium ions, but they do confirm the insertion of divalent ions into NiHCF.

NiHCF was cycled between 0.22 and 0.92 V versus SHE (standard hydrogen electrode) at 5C and retained 65, 53, 64, and 93% of initial capacity after 2000 cycles for  $\text{Mg}^{2+}$ ,  $\text{Ca}^{2+}$ ,  $\text{Sr}^{2+}$ , and  $\text{Ba}^{2+}$  electrolytes, respectively (Figure 3A–D). The capacity initially decays and then stabilizes over 2000 cycles (Figure 3A–D). This small decay is due to the partial solubility of NiHCF in the electrolyte. Adding a small concentration of 20 mM  $\text{Ni}^{2+}$  to the electrolyte before cycling begins solved this problem; the specific capacity and energy efficiency increased relative to results for cells without added  $\text{Ni}^{2+}$  (Figure 3E–H). The additional  $\text{Ni}^{2+}$  inserts into the electrode and stabilizes it, leading to an initial increase in capacity that levels out over time. This proposed mechanism has previously been observed for Cu-inserted CuHCF.<sup>39,40</sup> Evidence for reversible  $\text{Ni}^{2+}$  insertion in NiHCF can be found in the Supporting Information. Coulombic efficiency ranges from 99.4% for  $\text{Ca}^{2+}$  to 99.8% for  $\text{Mg}^{2+}$  and remains stable throughout cycling at 5C (Figure 3A–D). Round-trip energy efficiency reached 82, 83, 85, and 79% after 2000 cycles for  $\text{Mg}^{2+}$ ,  $\text{Ca}^{2+}$ ,  $\text{Sr}^{2+}$ , and  $\text{Ba}^{2+}$ , respectively. With additional  $\text{Ni}^{2+}$  in the electrolyte, the energy efficiency improved to 93, 91, and 89% for  $\text{Mg}^{2+}$ ,  $\text{Ca}^{2+}$ , and  $\text{Sr}^{2+}$ , respectively (Figure 3H). Energy efficiency is calculated based on a full cell voltage versus an activated carbon negative electrode.

Ex situ XRD spectra of NiHCF electrodes were collected with varying concentrations of different insertion cations corresponding to a range of charge states. The spectra were collected using a PANalytical X'Pert PRO Diffractometer with Cu- $K\alpha$  radiation; plots of the XRD results that confirm the phase stability of the materials with ion insertion can be found in the Supporting Information. The lattice parameter of each electrode increases with increasing charge state as cations are extracted from the lattice. From full discharge to full charge, the crystal increases in strain by 1.3, 1.1, and 0.9% for  $\text{K}^+$ ,  $\text{Mg}^{2+}$ , and  $\text{Ba}^{2+}$ , respectively (Figure 4). This increase in lattice parameter with charge is consistent with past studies<sup>27,28,41</sup> and is primarily due to the increase in diameter of  $\text{Fe}(\text{CN}_6)^{4-}$  upon oxidation to  $\text{Fe}(\text{CN}_6)^{3-}$ . This also explains why there is little

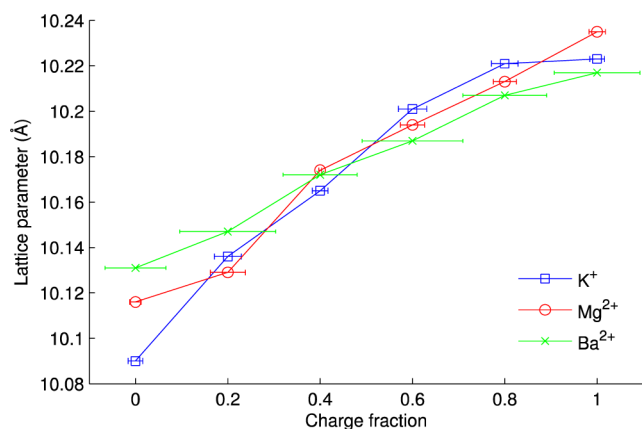


**Figure 4.** The increase in lattice parameter upon charging is not strongly dependent on the choice of insertion ion because the change in lattice parameter is primarily due to the increase in diameter of  $\text{Fe}(\text{CN}_6)^{4-}$  upon oxidation to  $\text{Fe}(\text{CN}_6)^{3-}$ . Uncertainties in lattice parameters are less than 0.001 Å.

difference in strain with cycling between different insertion ions. The open A sites in the structure are large enough to contain a variety of ions without distortion, which is why inserting ions with different diameters does not have a significant impact on crystal strain. The magnitude of strain upon full insertion of ions is very low ( $\sim 1\%$ ) and results in mechanical stability during cycling.

NiHCF nanoparticles can be easily synthesized with standard solution chemistry and low-cost precursors. These nanoparticles are highly crystalline, chemically stable, and possess a unique and versatile crystal structure that enables reversible insertion of a wide variety of different ions. Prior work has demonstrated the promise of hexacyanoferrate electrode materials in aqueous electrolyte batteries with monovalent cationic species. The present work shows that NiHCF, which has an open framework crystal structure, can also react with divalent insertion cations at high rates to produce unprecedented cycle life and Coulombic and energy efficiencies.

Exploration of other materials that allow reversible insertion of divalent ions (such as  $\text{Mg}^{2+}$ ) has proved to be difficult; increased electrostatic interaction between insertion ions and host atoms due to increased charge concentration can lead to slow kinetics, high voltage hysteresis, and poor cyclability.<sup>12,42,43</sup> Difficulty in redistributing the divalent charge to achieve local electroneutrality can also contribute to the poor kinetics of divalent insertion found in other experiments.<sup>43</sup>

On the other hand, a wide variety of monovalent and divalent ions can insert into NiHCF at high rates with low hysteresis. The mechanism has not been fully elucidated, but several hypotheses may help explain the observed electrochemical properties. The presence of hydrated ions and water molecules throughout the structure, both in A sites and coordinated to  $\text{Cu}^{2+}$  ions, can partially shield electrostatic interactions during diffusion in a manner analogous to water assisting  $\text{Mg}^{2+}$  insertion in  $\text{V}_2\text{O}_5$  electrodes.<sup>44</sup> Electrochemical impedance spectroscopy of  $\text{Mg}^{2+}$  in aqueous and organic electrolytes inserting into PB analogues supports the critical role of hydration in ion insertion.<sup>37</sup> Ordering of vacancies<sup>23</sup> and charge transfer between the host ions<sup>45,46</sup> can both redistribute concentrated charge effectively. Ferricyanide vacancies, which are roughly 5 Å in diameter and larger than the 3.2 Å interstitial A sites, may also assist insertion by providing additional diffusion paths for insertion ions.<sup>47</sup> The diffusion paths in these NiHCF nanoparticles are significantly shortened relative to electrodeposited PB analogues from past studies and contribute to rapid ionic diffusion. The combination of these features in PB open framework nanomaterials makes them uniquely suited for multivalent ion insertion. The versatility of the insertion reaction in NiHCF may make this material appropriate for a variety of applications in ion sensing, ion separation, and wastewater treatment.

The roles of zeolitic water, hydration shells around the insertion ions, ferricyanide vacancies, and hydronium ions in assisting the insertion process are not fully understood. Ongoing experiments in our group with synchrotron X-ray diffraction, extended X-ray absorption fine structure (EXAFS), neutron diffraction, and solid-state nuclear magnetic resonance (NMR) could provide a more complete understanding of the insertion reaction and its interaction with the local structure in NiHCF.

## ■ ASSOCIATED CONTENT

### Supporting Information

Electrochemical impedance spectroscopy of NiHCF in alkaline earth electrolytes; cyclic voltammogram of NiHCF cycled in  $\text{Ni}^{2+}$ ; XRD spectra of NiHCF with K, Mg, and Ba insertion ions. This material is available free of charge via the Internet at <http://pubs.acs.org>.

## ■ AUTHOR INFORMATION

### Corresponding Author

\*E-mail: [yicui@stanford.edu](mailto:yicui@stanford.edu).

### Author Contributions

R.Y.W. and Y.C. conceived the idea and designed electrochemical and physical experiments. R.Y.W. carried out and analyzed all material synthesis, electrochemical measurements, and physical characterization. C.D.W. helped with the initial experiments. R.A.H. participated in part of the discussion of the results. R.Y.W. and Y.C. prepared the manuscript. All authors read and made comments to the manuscript.

### Notes

The authors declare no competing financial interest.

## ■ ACKNOWLEDGMENTS

This work is supported by the Global Climate & Energy Project at Stanford University. R.Y.W. acknowledges support from the National Science Foundation Graduate Research Fellowship and the National Defense Science & Engineering Graduate Fellowship. We thank Dr. Mauro Pasta for his help with electrochemistry and experimental technique, and Dr. Badri Shyam and Dr. Johanna Nelson for their help with synchrotron X-ray diffraction.

## ■ REFERENCES

- (1) Tarascon, J.-M.; Armand, M. *Nature* **2001**, *414*, 359–367.
- (2) Ovshinsky, S. R.; Fetcenko, M. A.; Ross, J. *Science* **1993**, *260*, 176–181.
- (3) Goodenough, J. B.; Kim, Y. *Chem. Mater.* **2010**, *22*, 587–603.
- (4) Shukla, A.; Kumar, T. *J. Phys. Chem. Lett.* **2013**, *4*, 551–555.
- (5) Dunn, B.; Kamath, H.; Tarascon, J.-M. *Science* **2011**, *334*, 928–935.
- (6) Yang, Z.; Zhang, J.; Kintner-Meyer, M. C. W.; Lu, X.; Choi, D.; Lemmon, J. P.; Liu, J. *Chem. Rev.* **2011**, *111*, 3577–3613.
- (7) Soloveichik, G. L. *Annu. Rev. Chem. Biomol. Eng.* **2011**, *2*, 503–527.
- (8) Willems, J. *Philips J. Res.* **1984**, *39*, 1–91.
- (9) Mizushima, K.; Jones, P. C.; Wiseman, P. J.; Goodenough, J. B. *Mater. Res. Bull.* **1980**, *15*, 783–789.
- (10) Aurbach, D.; Lu, Z.; Schechter, A.; Gofer, Y.; Gizbar, H.; Turgeman, R.; Cohen, Y.; Moshkovich, M.; Levi, E. *Nature* **2000**, *407*, 724–727.
- (11) Aurbach, D.; Suresh, G. S.; Levi, E.; Mitelman, A.; Mizrahi, O.; Chusid, O.; Brunelli, M. *Adv. Mater.* **2007**, *19*, 4260–4267.
- (12) Levi, E.; Gofer, Y.; Aurbach, D. *Chem. Mater.* **2010**, *22*, 860–868.
- (13) Schöllhorn, R.; Kümpers, M.; Besenhard, J. O. *Mater. Res. Bull.* **1977**, *12*, 781–788.
- (14) NuLi, Y.; Yang, J.; Li, Y.; Wang, J. *Chem. Commun.* **2010**, *46*, 3794–3796.
- (15) Kegg, J. F.; Miles, F. D. *Nature* **1936**, *137*, 577–578.
- (16) Buser, H. J.; Schwarzenbach, D.; Petter, W.; Ludi, A. *Inorg. Chem.* **1977**, *16*, 2704–2710.
- (17) Itaya, K.; Uchida, I.; Neff, V. D. *Acc. Chem. Res.* **1986**, *19*, 162–168.
- (18) Herren, F.; Fischer, P.; Ludi, A.; Hälgl, W. *Inorg. Chem.* **1980**, *19*, 956–959.
- (19) Lee, H.; Kim, Y.-I.; Park, J.-K.; Choi, J. W. *Chem. Commun.* **2012**, *48*, 8416–8418.
- (20) Ludi, A.; Güdel, H. *Inorg. Chem.* **1973**, *14*, 1–21.
- (21) Widmann, A.; Kahlert, H.; Petrovic-Prelevic, I.; Wulff, H.; Yakhmi, J. V.; Bagkar, N.; Scholz, F. *Inorg. Chem.* **2002**, *41*, 5706–5715.
- (22) Bleuzen, A.; Escax, V.; Ferrier, A.; Villain, F.; Verdager, M.; Münsch, P.; Itié, J.-P. *Angew. Chem., Int. Ed.* **2004**, *43*, 3728–3731.
- (23) Flambard, A.; Köhler, F. H.; Lescouëzec, R. *Angew. Chem., Int. Ed.* **2009**, *121*, 1701–1704.
- (24) Ellis, D.; Eckhoff, M.; Neff, V. D. *J. Phys. Chem.* **1981**, *85*, 1225–1231.
- (25) Rajan, K. P.; Neff, V. D. *J. Phys. Chem.* **1982**, *86*, 4361–4368.
- (26) Itaya, K. *J. Appl. Phys.* **1982**, *53*, 804–805.
- (27) Wessells, C. D.; Huggins, R. A.; Cui, Y. *Nat. Commun.* **2011**, *2*, 550.
- (28) Wessells, C. D.; Peddada, S. V.; Huggins, R. A.; Cui, Y. *Nano Lett.* **2011**, *11*, 5421–5425.
- (29) Pasta, M.; Wessells, C. D.; Huggins, R. A.; Cui, Y. *Nat. Commun.* **2012**, *3*, 1149.
- (30) Matsuda, T.; Moritomo, Y. *Appl. Phys. Express* **2011**, *4*, 047101.
- (31) Lu, Y.; Wang, L.; Cheng, J.; Goodenough, J. B. *Chem. Commun.* **2012**, *48*, 6544–6546.
- (32) Asakura, D.; Okubo, M.; Mizuno, Y.; Kudo, T.; Zhou, H.; Ikeda, K.; Mizokawa, T.; Okazawa, A.; Kojima, N. *J. Phys. Chem. C* **2012**, *116*, 8364–8369.
- (33) Wang, L.; Lu, Y.; Liu, J.; Xu, M.; Cheng, J.; Zhang, D.; Goodenough, J. B. *Angew. Chem., Int. Ed.* **2013**, *52*, 1964–1967.
- (34) Wessells, C. D.; Peddada, S. V.; McDowell, M. T.; Huggins, R. A.; Cui, Y. *J. Electrochem. Soc.* **2012**, *159*, A98–A103.
- (35) Wessells, C. D.; McDowell, M. T.; Peddada, S. V.; Pasta, M.; Huggins, R. A.; Cui, Y. *ACS Nano* **2012**, *6*, 1688–1694.
- (36) Chen, S.-M. *J. Electroanal. Chem.* **2002**, *521*, 29–52.
- (37) Mizuno, Y.; Okubo, M.; Hosono, E.; Kudo, T.; Zhou, H.; Ohishi, K. *J. Phys. Chem. C* **2013**, *117*, 10877–10882.
- (38) Scholz, F.; Dostal, A. *Angew. Chem., Int. Ed.* **1996**, *34*, 2685–2687.
- (39) Guadagnini, L.; Tonelli, D.; Giorgetti, M. *Electrochim. Acta* **2010**, *55*, S036–S039.
- (40) Giorgetti, M.; Guadagnini, L.; Tonelli, D.; Minicucci, M.; Aquilanti, G. *Phys. Chem. Chem. Phys.* **2012**, *14*, 5527–5537.
- (41) Dostal, A.; Kauschka, G.; Reddy, S. J.; Scholz, F. *J. Electroanal. Chem.* **1996**, *406*, 155–163.
- (42) Amatucci, G. G.; Badway, F.; Singhal, A.; Beaudoin, B.; Skandan, G.; Bowmer, T.; Plitz, I.; Pereira, N.; Chapman, T.; Jaworski, R. *J. Electrochem. Soc.* **2001**, *148*, A940–A950.
- (43) Levi, E.; Levi, M. D.; Chasid, O.; Aurbach, D. *J. Electroceram.* **2007**, *22*, 13–19.
- (44) Novák, P.; Imhof, R.; Haas, O. *Electrochim. Acta* **1999**, *45*, 351–367.
- (45) Moritomo, Y.; Kato, K.; Kuriki, A.; Takata, M.; Sakata, M.; Tokoro, H.; Ohkoshi, S.; Hashimoto, K. *J. Phys. Soc. Jpn.* **2002**, *71*, 2078–2081.
- (46) Kim, J.; Tanaka, H.; Kato, K.; Takata, M.; Moritomo, Y. *Appl. Phys. Express* **2011**, *4*, 025801.
- (47) Moritomo, Y.; Igarashi, K.; Kim, J.; Tanaka, H. *Appl. Phys. Express* **2009**, *2*, 085001.